Analysis of Structural Features of Hard-Facing Overlays Performed Using Prototype Selfshielded Flux Cored Wires†

Robert A. BANKIEWICZ*, Kenji IKEUCHI***, Toshio ENJO**
and Yoshiaki ARATA**

Abstract

Hardfacing is of increasing importance in both reclamation and in strengthening of working surfaces. Determination of the serviceability of hard layers in various operating conditions requires a knowledge of their phase structure as well as the mode of overlays failure. Spectrochemical macroanalysis of hard layers showed desired composition of deposits and proved the correctness of the surfacing process. The hardness of layers reached 700 to 800 HV. Martensitic-austenitic structure with numerous precipitates was observed. EPMA and EDAX analyses disclosed an equal distribution of alloying elements without signs of segregation. Identification of the second phase was carried out using X-ray and EB diffraction analyses. Carbides and borides of alloying elements have been observed using TEM. SEM analysis of fracture morphology of overlays provided some information about the correlation of microstructural and fractographic features of several overlays. The outcomes of the reported investigations allow conclusions to be drawn about conditions of applicability of hardfaced overlays.

KEY WORDS: (Wearability) (Repair Welding) (Hardfacing) (Flux Cored Wire) (Precipitates Identification)

1. Introduction

The abrasive and impact-abrasive wear of working surfaces is a very important problem, among others in the building industry. Abrasion is the wearing away of surfaces by rubbing, grinding, or other types of friction, and is usually caused by the scouring action of earth, sand, gravel, slag, ballast and similar gritty materials. As regards building machines, the abrasive wear occurs on teeth, buckets, blades, and other high-mortality parts of earth movers, as well as on caterpillar undercarriages. Impact wear is a pounding type of wear that breaks, splits, crumbles and deforms metal surfaces in result of slamming contact with other hard surfaces or objects. Good examples are the impacts encountered by crushers hammers, tampers, and industrial heavy aggregate and concrete mixers. Both of these above mentioned types of wear occur in some combination with one another in the building machines and production plants. The wear life of the equipment parts depends on their material features as well as on their environmental and service conditions.

The effects of wear, which are very expensive because of downtime and part costs, can be reduced by means of surfacing with specialized welding filler metals that can provide more wear resistance than the underlying subsurface and considerably extend the usable life of parts.

It is now becoming popular for original equipment manufacturers to actually hardface wear parts on new equipment to provide its better service life[1].

The process using the flux cored wire, which is known as self-shielded arc welding, has the advantages of lower system maintenance costs, and of being able to weld with only simple torch and wire feeding device[2].

However, the proper selection of the hardfacing materials is very complex; the more so as there is a broad variety of rods and electrodes, including self-shielded flux cored wires. Further development of investigation and production in this range has been extended. On the other hand, with a few exceptions[3-4], there is no useful method of classifying and specifying hardfacing materials.

As is well known, the wearability of metallic alloys depends on their matrix structures, the distinctive features of precipitates and the coherence of the second phase with the matrix. The trybological phenomenon of wear and tear consists in transgranular and intergranular deterioration of lattice strengthened matrix, as well as in grind-

† Received on April 30, 1985
* Co-operative Researcher (Institute of Building Mechanization, Warsaw, Poland)
** Professor
*** Research Instructor

Transactions of JWRI is published by Welding Research Institute of Osaka University, Ibaraki, Osaka 567, Japan

ing and shearing of hardening precipitates and their tearing out of the matrix.

The reported work was undertaken to define the structural features of several hardfaced overlays faced using two prototype self-shielded flux cored wires. Simultaneously, another team has been carried out the laboratory wear tests and the field reliability tests of hardfaced excavators teeth, crusher hammers, and scraper blades of industrial concrete mixers. The comparison analysis of current examinations to complex wear tests will make possible to estimate the suitability of new core wires for hardfacing of machine parts in building industry, and will also be instrumental in improving the composition of the wires.

2. Experimental Procedure

2.1 Materials used

The overlayed material used was mild steel of St3s grade. The hardfacing filler materials used for semiautomatic arc surfacing were self-shielded flux cored wires named temporarily DR-11 and DR-14, according to pilot production numbering of wires. The designations and types of chemical composition of materials used are shown in **Table 1**.

Table 1 Chemical composition of material used.

Material	Chemical composition (wt %)										Remarks
	C	Si	Mn	P	S	Cr	Mo	Ti	Cu	B	
Base Metal: St3S-30 mm	0.14 0.22	0.12 0.30	0.35 0.60	max .05	max .05	max 0.3	max 0.3	max .02	max 0.2	-	Polish Standard: PN-58/H-84020
Selfshielded flux cored wire: DR-11 2.4 mm ø	0.50	1.0	0.60	-	-	9	0.6	0.15	-	-	Expected chemical composition of deposits
Selfshielded flux cored wire: DR-14 2.4 mm ø	0.80	0.9	-	-	-	13	-	-	3.7	1.6	

2.2 Surfacing process

The surfacing was performed utilizing MAGPOL-630DR type of semi-automatic tubular electrode welding euqipment. The welding parameters used were: arc Voltage 28-30 V, welding current – 280-310A, wire feeding speed – 250 mm/min.

The hardfacing consisted in multi-pass overlay welding, with application of one, two, and three-pad welds. In order to simplify the desired industrial process of hardfacing, neither preheating nor heat treatment were used.

The specimens for investegations were machined and next marked as: 11-1, 11-2, 11-3; 14-1, 14-2, 14-3, consequent upon designation of flux cored wires and the quantity of layers.

2.3 Chemical composition of deposits

The chemical analysis of areas close to face of surfacing overlays was performed utilizing GV-200 type Quantometer, and outcomes are shown in **Table 2.**

3. Experimental Results and Discussion

3.1 Hardness of overlays

The cross-sectional hardness distribution of overlays is illustrated in Figures 1 and 2.

Figure 1 reveals some resemblance of hardness distribution in cross-sections of one, two, and three-layers specimens which have been hardfaced using DR-11 wire. The most regular distribution of hardness, from the bond line to the overlay face appears in the one-layer speciment at the lowest, but predeterminated level of about 55 HRC. Due to the surfacing thermal cycle and the probable segregation of alloying elements, the fluctuation of hardness evidently occur in the fusion zones of the second and third layers. The hardness distribution in near overlay face areas of the two, and three-layer specimens are comparable with those occurring in one-layer specimens and spreads at least over a depth of 4mm.

Figure 2 shows characteristic hardness distribution of overlays executed using DR-14 wire which in principle is

Table 2 Chemical composition of surfacing layers.

Specimen	Chemical composition (wt %)							
	C	Si	Mn	Cr	Mo	Cu	Ti	B
11-1	0.27	0.72	0.70	4.54	0.38	-	0.08	-
11-2	0.36	0.95	0.70	6.36	0.54	-	0.11	-
11-3	0.43	0.92	0.63	7.33	0.61	-	0.14	-
14-1	0.57	0.65	-	8.49	-	1.93	0.78	
14-2	0.68	0.76	-	11.60	-	2.44	0.99	*)
14-3	0.73	0.80	-	12.77	-	2.77	1.11	

*) Boron indefinable

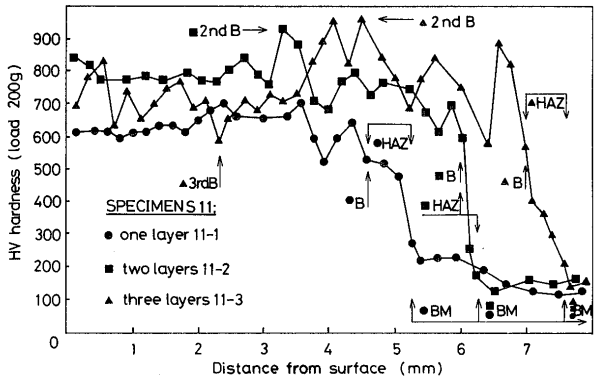

Fig. 1 Hardness distribution in cross-section of 11-1, 11-2 and 11-3 specimens.

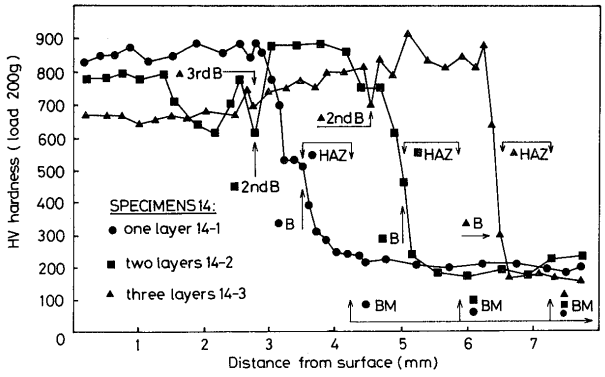

Fig. 2 Hardness distribution in cross-section of 14-1, 14-2 and 14-3 specimens.

similar form presented in Fig. 1, on condition that the highest hardness in near face areas of 14-series specimens occurs in one, two, and three-layers specimens, respectively.

In case of application to earth movers, the estimation of dimensions and properties of overlays is also essential in regards to the need for self-sharpening of the wearing parts. The thickness of strengthening layers has been found suitable for extention of wear life of working surfaces. On the other hand, as is well known, the hardness of metallic alloys is not equivalent to its wear resistance, especially in the metal to mineral wear and tear conditions; however, it is considered as some determinant of wearability.

In this connection, the complex determination of the overlays phase structure against a background of wear tests is necessary.

The advantage of self-shielded flux cored wire surfacing consists in its very low dilution coefficent, therefore may be apply for thin padding. Likewise, in reported case the base metal melting and diffusion appears not large, as is proven by the instantaneous drop of the hardness in HAZ of all specimens. More interesting in this regard, however, are the interrun fusion areas, which require application of particular investigation methods.

3.2 LM observations

In order to define a character of overlays microstructure, a routine optical microscopic examination has been carried out. As a premise to qualify the microstructure of overlays, both Shaeffler's diagram and numerous examples[5], as well as microhardness found have been taken into account.

Figure 3 shows martensitic-austenitic structure containing a large amount of precipitates within regions of grains. Specific for 11-series specimens microstructure is a high dilution level of first and second layer interfusion zone, as shown in Fig. 3(b, e); a very distinctive is also the weld fusion line of third layer appears in Fig. 3(c).

The hardfaced specimens of 14-series reveal austenitic-

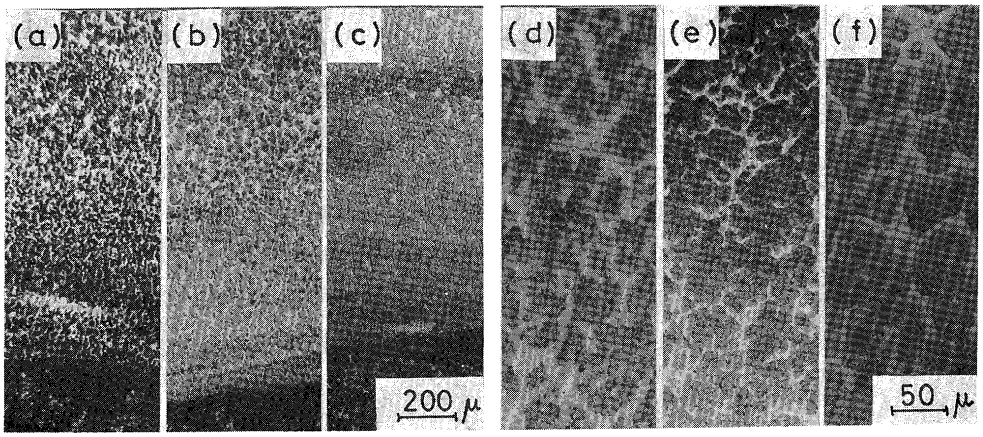

Fig. 3 Optical micrographs typical for 11-series overlays;
a) specimen 11-1: fusion boundary of one-pass layer,
b) specimen 11-2: first layer fusion boundary and second layer fusion zone,
c) specimen 11-3: fusion zone of second and third layers,
d) specimen 11-1: one-pass overlay,
e) specimen 11-2: first and second layers dilution area,
f) specimen 11-3: near face third layer.

martensitic structure with many fine precipitates at the boundaries of dendrites in columnar, equiaxed, vertical, and quasi-axial arrangement, as presented in **Fig. 4**. The most evident features of the fusion line areas of the multi-pass welds are the refinement of the second overlay structure, visible in Fig. 4(b, e), and some change of

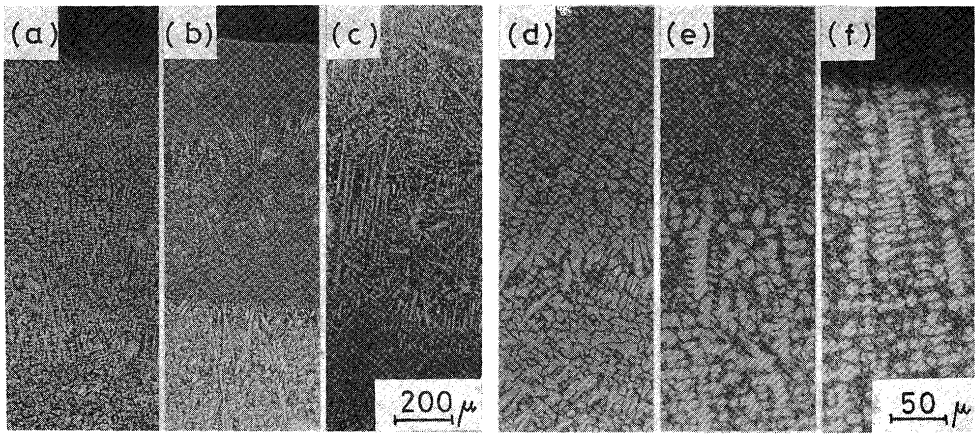

Fig. 4 Optical micrographs typical for 14-series overlays;
a) specimen 14-1: one-pass overlay,
b) specimen 14-2: first and second layers fusion zone,
c) specimen 14-3: second and third layers fusion zone,
d) specimen 14-1: near fusion boundary area of one-pass layer,
e) specimen 14-2: first and second layers fusion zone,
f) specimen 14-3: near face area of third layer.

crystalline orientation in the third layer, as seen in Fig. 4(c).

In accordance with applied chemical composition of wire cores, the observed microstructure met expected requirements for the matrix strengthening and for presence of precipitated phase. The morphology of hardening phase, its lattice disregistry and isostructuralism, chiefly determines the mechanism of overlays decohesion, and thus its serviceability.

3.3 Distribution of alloying elements

The investigation of alloying elements distribution in the crosssection of overlays was carried out to relate the effects of these concentration variables on structure and properties of the overlays.

Figures 5 and 6 show results of wave-length dispersive x-ray microanalysis (EPMA) of specimens 11-3 and 14-3.

The increase of Mo and Cr content in first, second, and third layers, respectively, is evident in 11-3 specimen and corresponds to outcomes of chemical macroanalysis of individual layers (Table 2).

The variation of content of alloying elements in each layer of 14-3 specimen seems less distinct then in the 11-3 specimen, with the exception of Cu-line. These differences of elements distribution have likewise close connection with results presented in Table 2 and will be discussed under fracture morphology of specimens.

However, the appearance of distinctive peaks is most

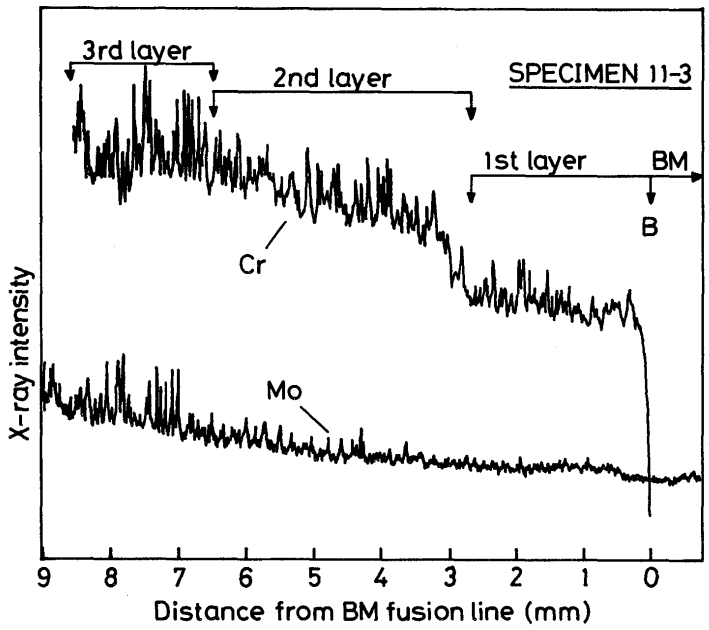

Fig. 5 EPMA results of Mo and Cr distribution in 11-3 specimen.

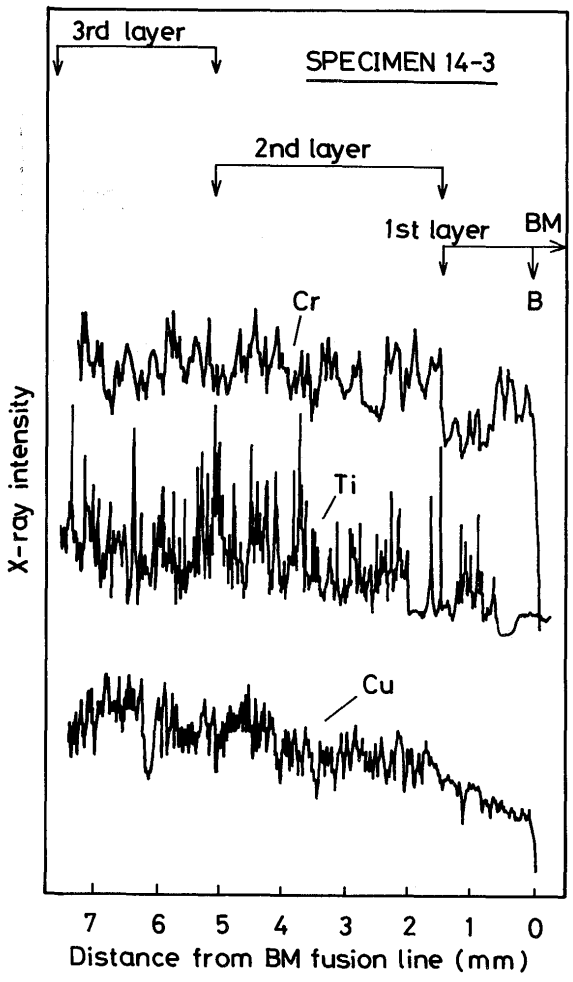

Fig. 6 EPMA results of Cu, Ti and Cr distribution in 14-3 specimen.

likely related to the displacement of alloying elements from the matrix and their concentration in the precipitates.

Energy dispersive x-ray microanalysis (EDAX) has been carried out with the purpose of evaluating elements distribution in selected structural areas of the overlays. The results of both line and point analyses are presented in Figures 7 and 8.

The investigated areas of 11-3 specimen have shown relatively low local nonuniformity, as illustrated in **Fig. 7.**

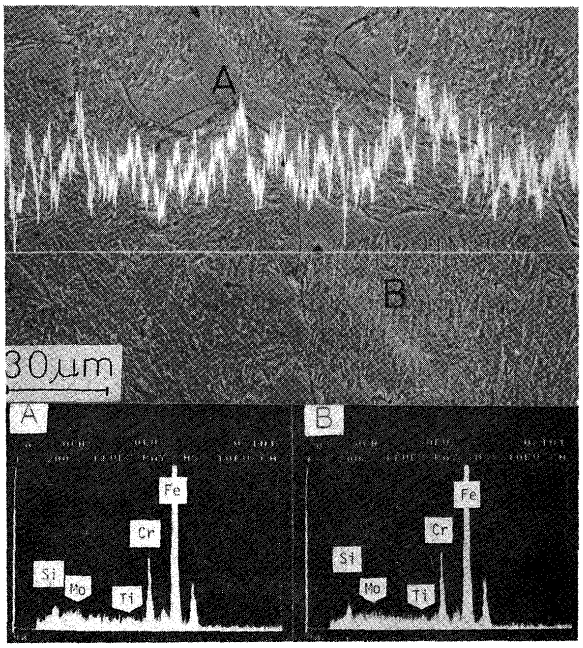

Fig. 7 Scanning electron micrograph and energy dispersive X-ray line analysis diagram of Cr along fusion zone of second and third layers of 11-3 specimen; EDAX patterns representative of the point analysis of the regions marked: A, B.

The variation of concentration of elements presented in **Fig. 8** evinces some connection with the course of scanned lines along differential microstructural regions of

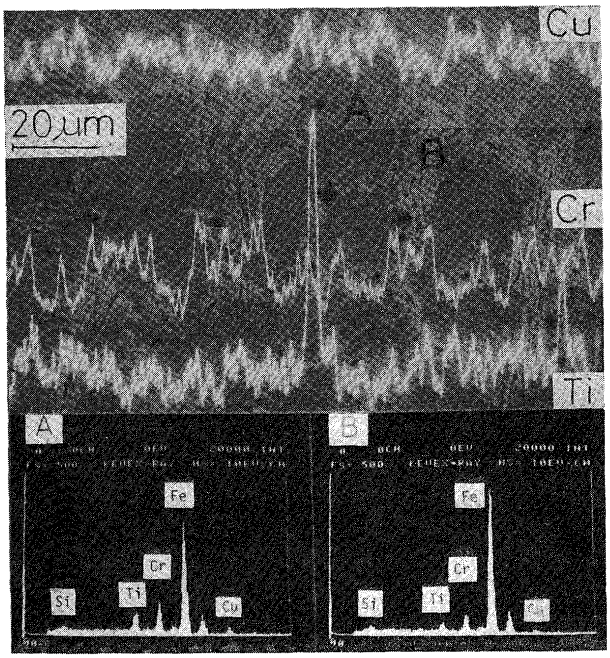

Fig. 8 Scanning electron micrograph and energy dispersive X-ray analysis diagrams of Ti, Cr and Cu along second layer area of 14-3 specimen; EDAX patterns representative of the point analysis of the regions marked: A, B.

specimen 14-3. In the areas defined in Fig. 4(f) as dendritic, a relative increase of alloying elements have been observed during the line analysis, as well as during point analysing (Fig. 8B).

Closer determination of the relationship between alloying elements distribution and substructural features of the overlays is not possible at this stage of investigation; neverthless, the information found will be an useful complement to data collection in this work.

3.4 Identification of precipitates

Recognition of the basic components of harfaced layers phase structure is one of pivotal items of the presented study. In this connection, x-ray structural analyses of individual layers, as well as electron-beam diffraction tests have been carried out.

Figure 9 and **10** show examples of x-ray structural analysis of 11-2 and 14-3 specimens. The complete results of these analyses are presented in **Table 3** and **4**.

The x-ray structural analysis of several layers was verified by electron-beam diffraction criteria by means of carbon extraction replicas, which have been taken from the very same areas of overlays.

TEM observations of extracted precipitates provided many indications of their nature and formation. The morphology of precipitates identified using TEM is illustrated representatively in **Figures 11** to **20**.

Table 5 lists all phases identified in both x-ray and electron-beam deffraction investigations.

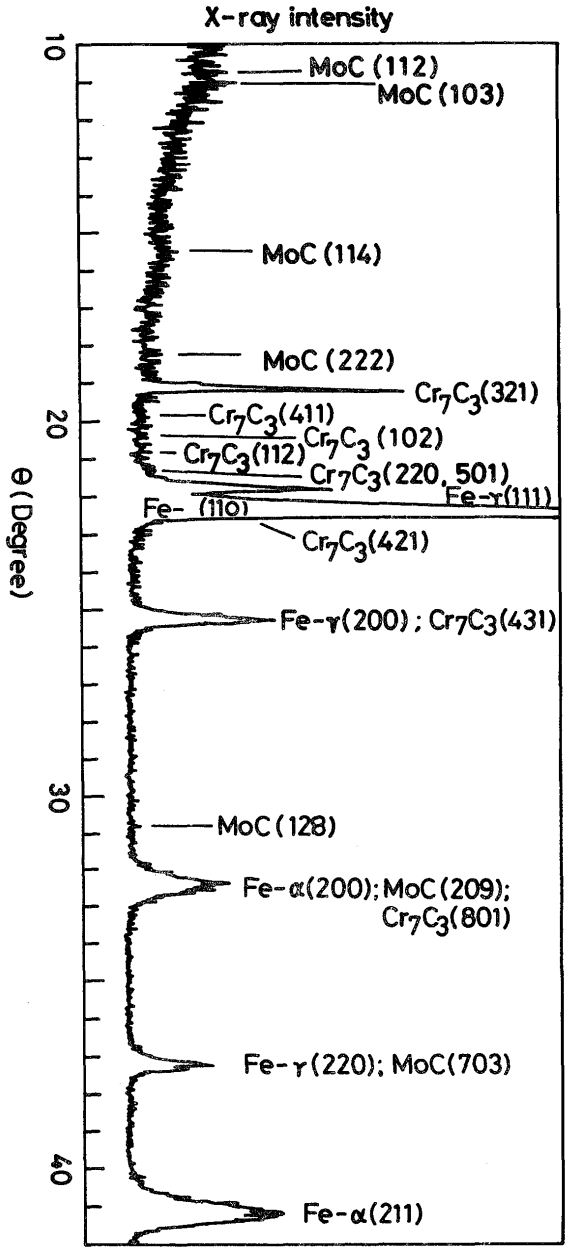

Fig. 9 Diagram of X-ray structural analysis of 11-2 specimen.

The correspondence of redoubled phase structure investigation results is clearly evident in Table 5, in spite of the fact that in some cases, detection of the precipitates by one method was not confirmed by the other.

Intentional chemical composition of wire cores has caused the appearance of numerous and of differential morphology precipitates in particular overlays. On the other hand, the structure of overlay matrices considered against the background of the above mentioned chemical composition shows alternating predomination of Fe-α and Fe-γ phases, most likely due to multipass thermal- and metallurgical processes of surfacing.

The various shape and sizes of precipitates were observed in TEM investigation and it was ascertained that

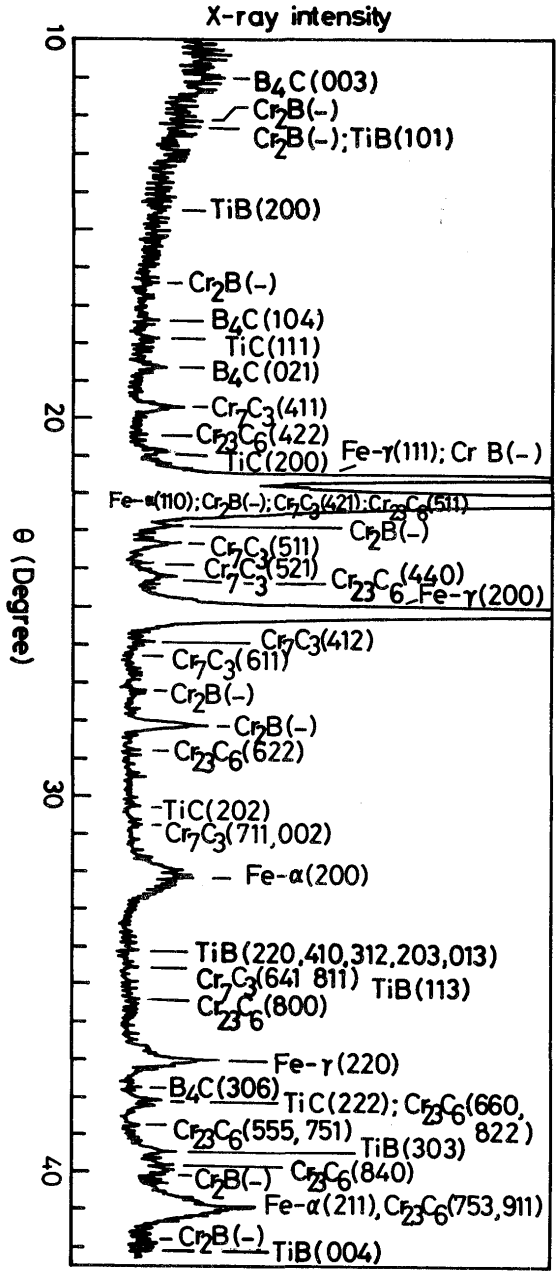

Fig. 10 Diagram of X-ray structural analysis of 14-3 specimen.

the favoured region for precipitation is the grain boundary (Figures 11 to 20). Fusiform, coagulated, rectangular and accicular shapes of precipitates, respectively, were the prevailing forms observed using TEM. The size of precipitated particles ranged from 0.1 μm (MoC, TiB) to 1.5 μm (Cr_7C_3).

The data from Table 5 regarding the lattice system and spacing allow some general estimation of lattice disregistry between each precipitate and Fe-α/Fe-γ matrices. This lattice disregistry, in connection with the state of phase boundaries coherence, determines the cohesion of overlays material. Besides the arrangement of precipitates and their coherence with parent lattice, the orientation of the precipitates towards the flow stress, as well as their shape,

Table 3 X-ray structural analysis of surfacing layers: 11-1, 11-2, 11-3.

Results		ASTM Data			
d Å	I/I_1	Type of Struct.	hkl	d Å	I/I_1
Specimen 11-1					
1.175	23	Fe-α	211	1.1702	30
1.440	12	Fe-α	200	1.4332	20
1.447	2	Cr_7C_3	801	1.44	70
1.488	2	Cr_7C_3	711,602	1.51	50
1.595	2	Cr_7C_3	531	1.62	60
1.803	3	Fe-γ	200		
		Cr_7C_3	431	1.81	100
1.969	3	Cr_7C_3	511	1.96	70
2.031	100	Fe-α	110	2.0283	100
		MoC	410	1.998	30
		Cr_7C_3	421	2.04	100
2.204	2	Cr_7C_3	102	2.22	70
2.261	2	Cr_7C_3	411	2.28	70
2.431	2	MoC	222	2.45	70
3.489	3	MoC	210	3.47	100
4.057	8	MoC	103	4.00	100
Specimen 11-2					
1.171	21	Fe-α	211	1.1702	30
1.247	12	Fe-γ	220		
		MoC	703	1.258	30
1.438	20	Fe-α	200	1.4332	20
		MoC	209	1.414	50
		Cr_7C_3	801	1.44	70
1.507	3	MoC	128	1.506	30
		Cr_7C_3	711,602	1.51	50
1.804	20	Fe-γ	200		
		Cr_7C_3	431	1.81	70
2.034	100	Fe-α	110	2.0286	100
		Cr_7C_3	421	2.04	100
2.082	25	Fe-γ	111		
2.131	4	Cr_7C_3	220,501	2.12	70
2.171	4	Cr_7C_3	112	2.14	50
2.272	4	Cr_7C_3	411	2.28	70
2.348	30	Cr_7C_3	321	2.35	20
2.462	6	MoC	222	2.45	70
2.887	8	MoC	114	2.83	30
4.017	14	MoC	103	4.00	100
4.140	14	MoC	112	4.17	100
Specimen 11-3					
1.175	34	Fe-α	211	1.1703	30
1.247	8	Fe-γ			
1.144	16	Fe-α	200	1.4332	20
1.695	3	Cr_7C_3	611	1.71	60
1.752	3	Cr_7C_3	412	1.75	70
1.807	21	Fe-γ			
1.918	5	Cr_7C_3	222	1.90	50
1.993	7	MoC	410	1.998	30
2.038	100	Fe-α	110	2.0268	100
		Cr_7C_3	421	2.04	100
2.080	19	Fe-γ	111		
2.151	4	Cr_7C_3	112	2.14	50
2.222	7	Cr_7C_3	102	2.22	50
2.265	7	Cr_7C_3	411	2.28	70
2.362	87	Cr_7C_3	321	2.35	20
2.477	7	MoC	222	2.45	70
2.834	8	MoC	114	2.830	30
3.463	8	MoC	210	3.47	100
4.020	12	MoC	103	4.00	100
4.166	12	MoC	112	4.17	100

Table 4 X-ray structural analysis of surfacing layers: 14-1 and 14-2.

Results		ASTM Data				Results		ASTM Data			
d Å	I/I_1	Type of Struct.	hkl	d Å	I/I_1	d Å	I/I_1	Type of Struct.	hkl	d Å	I/I_1
Specimen 14-1											
1.173	16	Fe-α	211	1.1702	30	1.276	12	Fe-γ	220		
1.192	7	Cr_2B	-	1.192	50	1.306	2	TiC	311	1.305	5
1.218	3	$Cr_{23}C_6$	555,751	1.231	90	1.322	3	B_4C	223	1.326	20
1.272	3	$Cr_{23}C_6$	660,822	1.256	100	1.339	2	Cr_7C_3	641,811	1.33	50
		Fe-γ				1.372	2	TiB	220,410	1.362	72
1.310	3	$Cr_{23}C_6$	644,822	1.293	60				313,203		
1.317	3	$Cr_{23}C_6$	800	1.333	40				013		
1.342	2	$Cr_{23}C_6$	641,811	1.35	80	1.435	4	Cr_7C_3	810	1.44	70
1.444	9	Fe-α	200	1.4332	20	1.444	6	Fe-α	200	1.4332	20
		Cr_7C_3	801	1.44	70			Cr_7C_3	801	1.44	70
1.505	2	Cr_7C_3	711,602	1.51	50	1.456	4	TiB	401	1.461	28
1.526	3	TiC	202	1.531	11	1.475	4	$Cr_{23}C_6$	604	1.48	5
1.631	3	Cr_2B	-	1.649	100	1.494	4	Cr_2B	-	1.489	20
1.756	5	Cr_7C_3	412	1.75	70	1.541	4	TiC	220	1.531	11
1.779	3	Cr_7C_3	521	1.78	50	1.628	8	Cr_2B	-	1.649	100
1.800	6	Fe-γ	200			1.663	3	Cr_2B	-	1.678	10
1.889	3	$Cr_{23}C_6$	440	1.88	50	1.705	3	Cr_7C_3	611	1.71	60
1.938	3	Cr_2B	-	1.95	50	1.746	3	Cr_7C_3	412	1.75	70
1.973	7	Cr_7C_3	511	1.96	70	1.807	60	Fe-γ	200		
2.033	100	Fe-α	110	2.0268	100	1.883	4	$Cr_{23}C_6$	440	1.88	50
		Cr_7C_3	421	2.04	100	1.943	5	Cr_2B	-	1.95	50
2.169	5	TiC	200	2.166	100	1.973	6	Cr_7C_3	511	1.96	70
2.287	5	Cr_7C_3	411	2.28	70	2.038	68	Fe-α	110	2.0268	100
2.392	6	B_4C	021	2.38	100			Cr_2B	-	2.038	100
2.569	3	B_4C	104	2.57	80			Cr_7C_3	421	2.04	100
2.931	4	Cr_2B	-	2.93	50			$Cr_{23}C_6$	511	2.05	100
3.775	4	B_4C	012	3.79	70	2.085	100	Fe-γ	111		
Specimen 14-2								Cr_2B	-	2.107	100
						2.153	4	TiC	200	2.166	100
1.144	3	TiB	004	1.141	12			TiB	102	2.14	100
1.150	3	Cr_2B	-	1.160	100	2.202	4	$Cr_{23}C_6$	422	2.17	50
1.177	8	Fe-α	211	1.1702	30	2.270	6	Cr_2B	-	2.286	90
		$Cr_{23}C_6$	753,911	1.170	90	2.398	3	B_4C	021	2.38	100
1.188	6	TiB	501,321	1.181	28	2.502	3	TiC	111	2.50	14
1.193	6	Cr_2B	-	1.192	50	2.572	4	B_4C	104	2.57	80
1.196	6	Cr_2B	-	1.209	80	2.709	4	Cr_7C_3	311	2.68	20
1.227	3	$Cr_{23}C_6$	555,751	1.231	90	2.912	4	Cr_2B	-	2.93	50
1.249	3	TiC	222	1.250	5	3.051	4	TiB	200	3.053	32
1.255	3	$Cr_{23}C_6$	660,822	1.256	100	3.549	4	Cr_2B	-	3.57	20
						3.626	6	TiB	101	3.633	20
						3.775	4	B_4C	012	3.79	70
						4.072	6	B_4C	003	4.02	40

Table 4 (cont.) X-ray structural analysis of 14-3 specimen third layer.

Results		ASTM Data				Results		ASTM Data			
d Å	I/I_1	Type of Struct.	hkl	d Å	I/I_1	d Å	I/I_1	Type of Struct.	hkl	d Å	I/I_1
1.148	5	TiB	004	1.141	12	1.709	4	Cr_7C_3	611	1.71	60
1.154	5	Cr_2B	-	1.160	100	1.760	5	Cr_7C_3	412	1.75	70
1.175	20	Fe-α	211	1.1702	30	1.807	100	Fe-γ	200		
		$Cr_{23}C_6$	753,911	1.170	90	1.880	8	$Cr_{23}C_6$	440	1.88	50
1.199	8	Cr_2B	-	1.192	50	1.903	5	Cr_7C_3	521	1.90	50
1.202	8	$Cr_{23}C_6$	840	1.192	80	1.941	8	Cr_7C_3	511	1.96	20
1.211	8	TiB	303	1.219	16	2.033	87	Fe-α	110	2.0286	100
1.228	5	$Cr_{23}C_6$	555,751	1.231	90			Cr_2B	-	2.038	100
1.247	6	TiC	222	1.250	5			Cr_7C_3	421	2.04	100
		$Cr_{23}C_6$	660,882	1.256	100			$Cr_{23}C_6$	511	2.05	100
1.263	5	B_4C	306	1.261	20	2.089	74	Fe-γ	111		
1.273	13	Fe-γ	220					Cr_2B	-	2.107	100
1.329	5	$Cr_{23}C_6$	800	1.330	40	2.154	7	TiC	200	2.166	100
1.343	5	TiB	113	1.331	24	2.202	4	$Cr_{23}C_6$	422	2.17	50
1.356	5	Cr_7C_3	641,811	1.35	80	2.280	8	Cr_7C_3	411	2.28	70
1.371	5	TiB	220,410	1.362	72	2.398	7	B_4C	021	2.38	100
			312,203			2.502	6	TiC	111	2.500	14
			013			2.569	6	B_4C	104	2.57	80
1.448	10	Fe-α	200	1.4332	20	2.724	6	Cr_2B	-	2.71	10
		Cr_7C_3	801	1.44	70	3.065	8	TiB	200	3.056	32
1.505	4	Cr_7C_3	711,602	1.51	50	3.604	10	Cr_2B	-	3.57	20
1.526	4	TiC	202	1.531	11			TiB	101	3.633	20
1.599	4	$Cr_{23}C_6$	622	1.61	30	3.670	10	Cr_2B	-	3.65	20
1.631	11	Cr_2B	-	1.649	100	4.057	12	B_4C	003	4.02	40
1.683	4	Cr_2B	-	1.678	10						

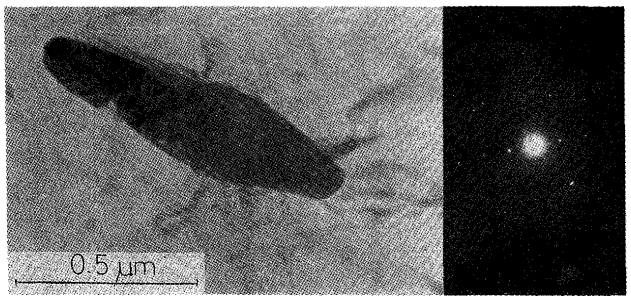

Fig. 11 Specimen 11-2: TEM micrograph of Mo_2C carbide located in the second layer, (Carbon Extraction Replica – CER).

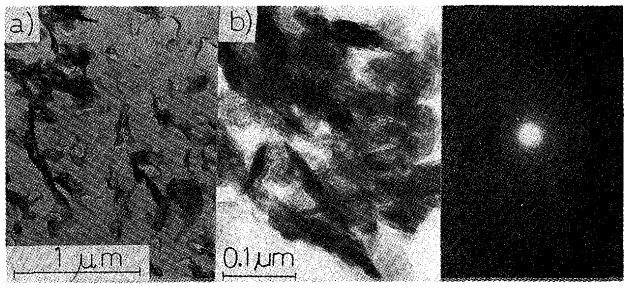

Fig. 12 Specimen 11-3: TEM micrograph showing MoC carbides at the grain boundaries of third layer (a); (b) - fragment of (a) - area (CER).

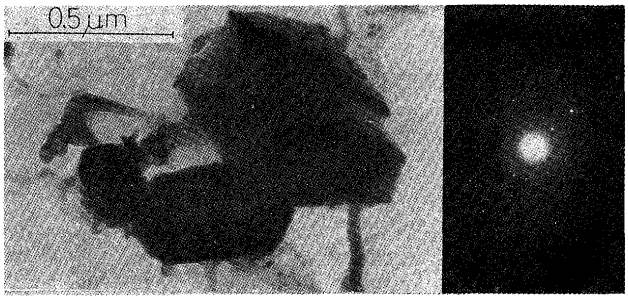

Fig. 13 Specimen 11-3: TEM micrograph showing $Cr_{23}C_6$ carbides coalesced at the grain boundaries of second layer (CER).

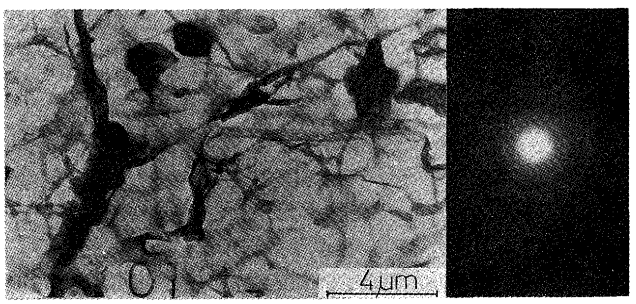

Fig. 14 Specimen 11-3: TEM micrograph showing Cr_7C_3 carbides at the grain boundaries of second layer (CER).

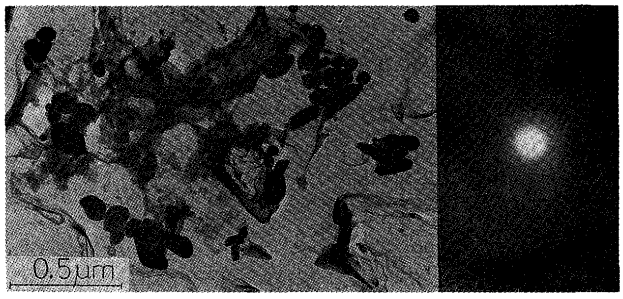

Fig. 15 Specimen 14-2: TEM micrograph showing coagulated borides situated at the grain boundaries of second layer (CER).

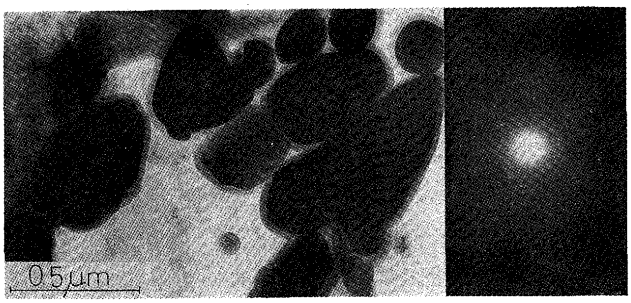

Fig. 16 Specimen 14-3: TEM micrograph of coagulated Cr_2B borides located at the grain boundaries of second layer (CER).

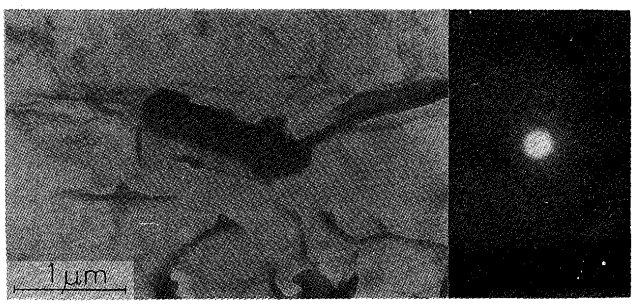

Fig. 17 Specimen 14-3: TEM micrograph of $CR_{23}C_6$ carbides situated at the grain boundary of second layer (CER).

Fig. 18 Specimen 14-3: TEM micrograph of Cr_7C_3 carbide situated at the first layer grain boundary (CER).

Fig. 19 Specimen 14-3: TEM micrograph of TiC carbide situated at third layer grain boundary (CER).

Fig. 20 Specimen 14-3: TEM micrograph of TiB boride situated at third layer grain boundary (CER).

Table 5 Results of phase structure investigations.

Type of Phase	System	Lattice Parameters Å	Region of identification using diffraction of: X-ray(X); elektron beam(E)					
			11-1	11-2	11-3	14-1	14-2	14-3
Fe- α	Cubic	(found)	X† 2.876	X† 2.880	X† 2.888	X† 2.888	X 2.888	X 2.896
Fe- γ	Cubic	(found)	X 3.606	X 3.608	X 3.614	X 3.600	X† 3.614	X† 3.614
Cr_7C_3	Hexag.	↓ASTM↓ a_o-13.98 c_o- 4.523	X	X,E	X,E	X	X,E	X,E
$Cr_{23}C_6$	Cubic	a_o-10.638	-	-	-	X	X	X,E
Cr_2B	-	-	-	-	-	X	X	X,E
TiC	Cubic	a_o- 4.330	-	-	-	X	X	X,E
TiB	Orth.	a_o- 6.12 b_o- 3.06 c_o- 4.56	-	-	-	-	X,E	X,E
B_4C	Hexag.	a_o- 5.61 c_o-12.07	-	-	-	X	X	X,E
MoC	Hexag.	a_o-10.60 c_o-13.39	X	X,E	X,E	-	-	-
Mo_2C	Hexag.	a_o- 2.994 c_o- 4.722	-	E	-	-	-	-
Fe_2MoC	Orth.	a_o-16.27 b_o-10.03 c_o-11.32	-	E	-	-	-	-

† - highest peak

greatly affect the cohesive strength of overlays. In this regards, the oblong second-phase particles are more dangerous stress concentrators than a spherulites.

The final determination as to which of the found precipitates are coherent with the matrix is very complex, but the most likely MoC, TiC, and TiB may be considered as most coherent with their matrices.

3.5 Morphology of fractured surfaces

SEM fractography of overlays was conducted in order to distinguish some basic features of hardfaced layers decohesion process.

The fracture surfaces for SEM observations were obtained in result of very slow bending of notched speciments. Fracture morphology was nor always significantly connected with both hardness and alloying elements distribution.

The typical fracture mode of the areas close to the bond of 11-1, 11-2, and 11-3 speciments was transcrystalline cleavage fracture. The fracture surfaces consisted of

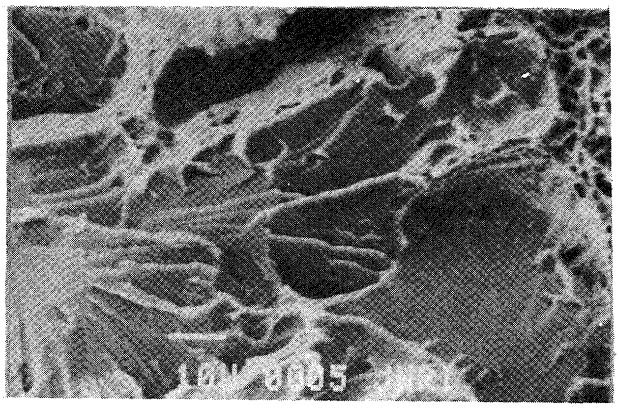

Fig. 21 SEM fractograph of area close to bond of 11-1 specimen.

many facets and were mainly characterized by fan-shaped patterns as shown in **Fig. 21**. At the upper right-hand corner, ductile fracture characteristic of the central area of 11-1 specimen has occurred.

Further observations conducted up to the face of 11-1 specimen overlay disclosed an equal mixture of cleavage-like facets and many dimples as can be seen in **Fig. 22**.

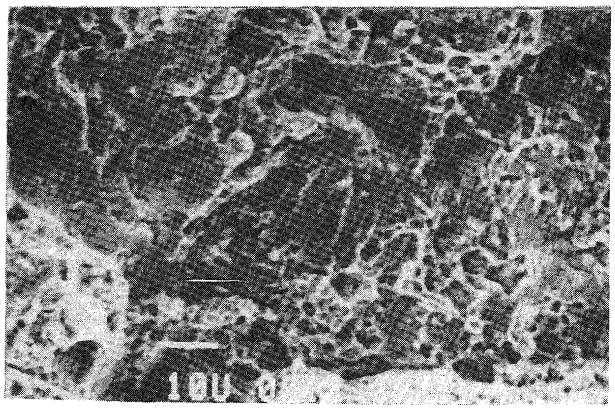

Fig. 22 SEM fractograph of area close to face of 11-1 specimen.

The topography of 11-1 specimen has not shown any signs of secondary cracks and did not manifest traces of intercrystalline failure.

While estimating the fracture morphology and the effect of precipitates on the mechanism of failure[6, 8] were considered.

The area close to bond of 11-2 and 11-3 specimens disclosed identical character like the same area of 11-1 specimen, as can be seen in Fig. 21. The cleavage fracture of these areas corresponds with an evident increase of hardness, undoubtedly caused by rapid heat transfer to the cold base metal.

The prominent feature of other 11-2 specimen areas is the presence of secondary cracks, most likely caused by precipitates situated at the grain boundaries as is visible in **Figs. 23** and **24**.

Figures 23 and 24 show ductile dimple and quasi-

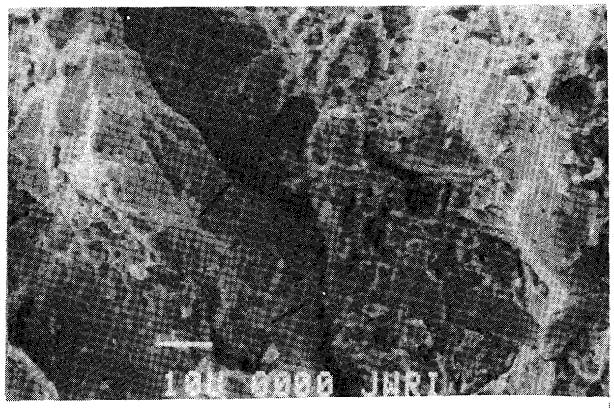

Fig. 23 SEM fractograph of first layer of 11-2 specimen.

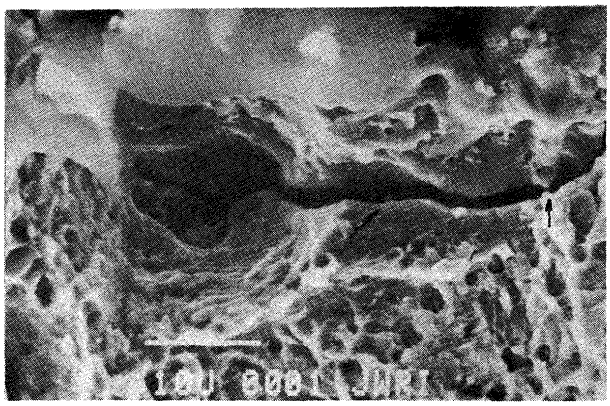

Fig. 24 SEM fractograph of second layer of 11-2 specimen.

cleavage fracture character of 11-2 specimen and exemplify the secondary cracks.

The fracture morphology of 11-3 specimen revealed a great similarity to observed in the 11-2 specimen. The significant common feature is appearance of secondary cracks as illustrated clearly in **Fig. 25**. The presence of

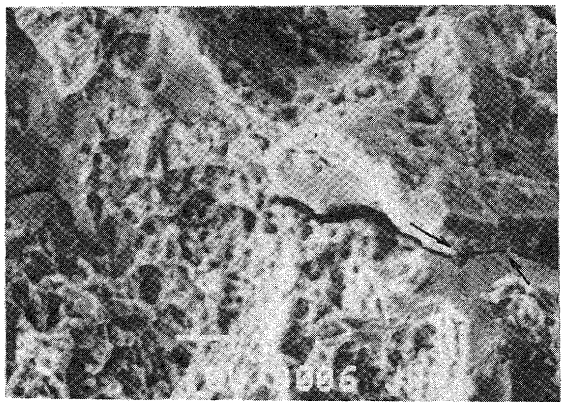

Fig. 25 SEM fractograph of second and third layers fusion area of 11-3 specimen.

precipitates at the grain boundaries corresponds with TEM micrograph of the same speciment (Fig. 14).

The presence of secondary cracks is caused most likely by an increase of Cr and C content found in the second and third layers. The occured chromium carbides located at the grain boundaries raise the level of internal stresses

of the martensitic-austenitic structure.

SEM examinations of 14-series specimens have shown high uniformity of their fracture morphology. Transcrystalline cleavage fracture of the area close to bond of 14-1 specimen, as well as the characteristics of the dendrite structure ductile rupture mode of the other regions of the overlay are shown in **Figures 26** and **27**.

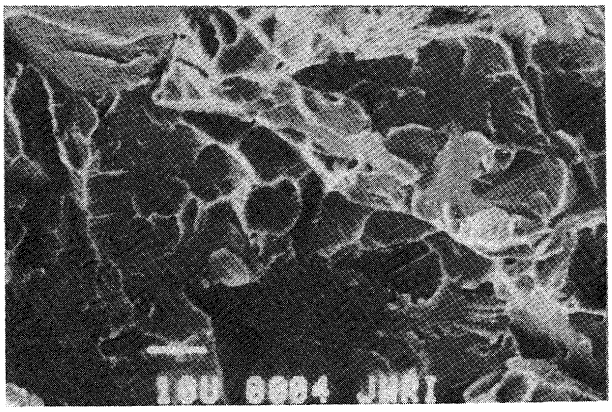

Fig. 26 SEM fractograph of area close to bond of 14-1 specimen.

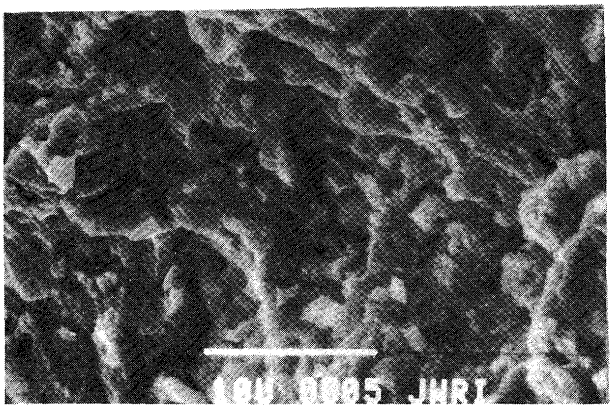

Fig. 27 SEM fractograph of the centre of 14-1 specimen overlay.

The topography presented in Figs. 26 and 27 is representative for 14-series and shows some connection with both the hardness and alloying elements distribution.

4. Summary and Conclusions

The expected features of hardfacing layers, which have been surfaced using two prototype self-shielded flux cored wires, were partly confirmed by the investigations conducted.

The interaction of various factors during formation of hard surfaces frustrates the precise analysis of the individual importance of those factors, necessary to optimize the hardfacing process. If we assume that the range of self-shielded hardfacing parameters adjustment is very narrow, then only the modification of wire core composition may influence the effects of the process, or the heat treatment previously rejected.

The chemical macroanalysis of individual layers shows the desired constitution of deposited metals. It provides on how the selfshielding of used wires could be employed to assure the course of correct metallurgical processes and maximum passage of alloying elements to the overlay.

The obvious proof of prospective wear resistance structure formation, is the very high hardness of all layers. The found hardness corresponds, as one of wearability indexes, with the observed martensitic-austenitic structure with numerous precipitates. The presence of martensite was confirmed by the appearance of characteristic peaks of Fe-α (200) as well as by the increase of Fe-α lattice parameters. The martensitic structure is advantageous in regard to the abrasion hardness, but on the other hand, is dangerous due to its high level of internal stresses; illustrative examples are intercrystalline cracks observed in 11-2 and 11-3 specimens.

The alloying elements distribution in overlays is rather uniform and provides no evidence of apparent segregation. The existent disposition of alloying elements causes both the strengthening of the parent lattice as well as precipitation strengthening of deposits. Positive action may be credited to copper and boron employed in DR-14 wire composition. Copper as an austenite stabilizer limits the formation of martensite owing to the rising of stacking fault energy of austenite; moreover, the positive effect of copper on the mechanical properties of iron alloys, in particular due to sinergistic effect of chromium[7] is well known. Boron forms an interstitial solution which causes strengthening of the austenite lattice comparable in intensity only to the action of carbon and nitrogen. The appearance of hard titanium and chromium borides, considered in general as coherent with a matrix of iron alloys, is also valuable.

Neverthless, it is difficult to ascertain unequivocally whether the precipitates of the observed morphology are suitable to predetermined service conditions of hardfaced layers. It cannot be differentiated at this present stage of investigation, except where there is an obvious association of secondary cracks with the presence of Cr_7C_3-chromium carbides at the grain boundaries. Estimation of conceivable harmful effect of above mentioned large carbides and of the spalling resistance of multi-pass deposits, which were hardfaced using DR-11 wire will be possible after completion of the field tests.

For the complex definition of substructural features of several overlays, however, an investigation which can provide more information about interphase boundaries of deposits would be advisable. Furthermore, for an optimization of overlays structure and properties, some closer knowledge of precipitates nucleation, growth and transformation phenomena is necessary.

The final purpose of investigation of hardfacing is to

make possible the formation of a matrix with a range of desired ductility, and with a fine well-dispersed second phase, providing an effective differential mechanism of dislocation locking.

The observations, results and discussions presented here can provide some information in characterizing the features and applicability of deposits which have been hardfaced using two prototype self-shieded flux cored wires.

The major conclusions can be summarized as follows.

1. These hardfaced overlays are highly suitable to work in conditions of metal-to-mineral surface contact.
2. Owing to the characteristics of the hardfacing process used, the sufficient wearability can be obtained in one-pass overlay welding.
3. The overlays which have been hardfaced using DR-11 wire can be applied to the work in abrasive wear service conditions. In case of impact-abrasive wear, preheating, heat treatment or both preventive treatments are recommended to increase the ductility of multi-pass overlays.
4. The overlays which have been hardfaced using DR-14 wire can be applied to the impact-abrasive operating conditions due to the structural features of strengthened austenite.
5. It is necessary to compare and contrast these reported investigations with quantitive outcomes of both wear and field tests.

Acknowledgement

The authors would like to express their appreciation to Assoc. Professor Dr. Yasushi Kikuchi and Dr. Toshio Kuroda from the Welding Research Institute of Osaka University for their stiumlating discussion during the course of investigations reported here.

References

1. Hovard B. Cary: Modern Welding Technology, Prentice-Hall Inc., N. York, 1979.
2. F. Matsuda et al.: Trans. of JWRI, Vol. 12. No. 1 (1981). p. 19.
3. "Welding and Brazing", Metals Handbook, Vol. 6, 8th Edition (Chapter on Hardfacing by Welding), ASM Metals Park, Ohio.
4. Lester F. Spencer: Hardfacing, Picking the Proper Alloy, The Welding Engineer, Nov. 1970, Chicago, Illinois.
5. Metallographic Atlas, Japan Welding Society, 1984.
6. L. Engel, H. Klingele: Metal Demage, Carl Hanser Verlag, Munich-Vienna, 1981.
7. F. Staub et al.: Metaloznawstwo, "Slask"-Katowice, 1973 (in Polish).
8. "Fractography in Failure Analysis", ASTM, Philadelphia, Pa,. 1977.